



In situ synthesis of ZnO/ZnTe common cation heterostructure and its visible-light photocatalytic reduction of CO₂ into CH₄



Muhammad Fahad Ehsan^{a,b}, Tao He^{a,*}

^a Laboratory of Nanosystem and Hierarchical Fabrication, National Center for Nanoscience and Technology, Beijing 100190, China

^b University of Chinese Academy of Sciences, Beijing 100049, China

ARTICLE INFO

Article history:

Received 20 September 2014

Received in revised form

26 November 2014

Accepted 30 November 2014

Available online 3 December 2014

Keywords:

ZnTe

ZnO

Common cation heterostructure

CO₂ photoreduction

CH₄

ABSTRACT

The development of hierarchical superstructures and their application for the sake of clean and sustainable energy is an attractive research field. Here we reported in situ synthesis of common cation heterostructure via modification of zinc oxide (ZnO) by zinc telluride (ZnTe) photocatalyst through one-pot hydrothermal approach at reaction temperature of 180 °C. The phase, crystal structure, morphology, composition, optical property and alignment of energy levels of the as-synthesized ZnO/ZnTe heterostructure have been thoroughly studied by different techniques. The heterostructure fabricated with different ZnO flower-like nanostructures (hundreds of nanometers for the rod length or sheet size of the petals and tens of nanometers for the corresponding diameter or thickness) exhibited different photocatalytic capability for reduction of carbon dioxide into methane under visible-light irradiation ($\lambda \geq 420$ nm), which is mainly due to the different exposed crystal planes of ZnO and different surface area (15.0 and 5.6 m² g⁻¹ for sheet-like petals and rod-like petals, respectively). The obtained photocatalytic systems show good visible-light photoreduction capability even with ~3.35% ZnTe in terms of atomic percentage, for which the solar energy conversion efficiency can reach ~3.28% in the first 30 min of photoreduction. The formation of heterojunction can facilitate charge transfer and thus improve the photocatalytic activity. In addition, the advantage of sharing common cations for a heterostructure is also briefly discussed.

© 2014 Elsevier B.V. All rights reserved.

1. Introduction

It has long been discussed in a comprehensive way over the past few decades and has already been accepted as a point of agreement that the consumption of fossil fuels has serious limitations on the global scale. As a direct result of their combustion, the increase in the level of atmospheric carbon dioxide (CO₂) has caused serious concerns about global warming [1,2], and thereby, its effective fixation would definitely benefit the mankind for the sake of a sustainable society. To solve this problem, so far the focus has been on the technology development for CO₂ capture and storage. But only a very few percentage of the captured CO₂ can be converted into valuable products. As a result, the development of new routes for the CO₂ conversion via production of value-added products like fuels [3,4] has become an attractive field of the materials [5–8]. To achieve this target, artificial photosynthesis seems to be an efficient approach for the production of solar fuels from the reduction of CO₂ [9–11].

Some materials like metal oxides [12–15], tantalates [16], ZnGa₂O₄ [17], Zn₂GeO₄ [18,19] and titanium-based materials [20–22] have been used as the photocatalysts for the CO₂ photoreduction because of their suitable band gap and convenient band positions against standard hydrogen electrode (SHE) for the production of different solar fuels (such as methane, carbon monoxide and methanol). However, the utilization of such a single semiconductor material as photocatalyst is often restrained by its short lifetime of photogenerated electron–hole pairs, photocorrosion, and insufficient utilization of solar energy due to its large band-gap. On the other hand, the narrow-band-gap semiconductors are able to absorb visible-light photons for the generation of electron–hole pairs, while unfortunately suffer from the fast recombination of these charge carriers. Therefore, it is a vital concern to develop a rational design for the fabrication of nanostructured photocatalysts that can exhibit high activity with efficient charge separation and visible-light utilization for the practical applications.

Amongst a variety of the semiconductors used for the photoreduction of CO₂ hitherto, titanium dioxide (TiO₂) is one of the most widely used photocatalytic materials [23–25]. In contrast to TiO₂, zinc oxide (ZnO) is an n-type semiconductor with a direct band gap of ~3.3 eV, and is similar to TiO₂ in terms of its band gap and band

* Corresponding author. Tel.: +86 1082545655; fax: +86 1062656765.

E-mail address: het@nanocr.cn (T. He).

Table 1
Reaction conditions for the synthesis of different products.

Sample	[Zn(NO ₃) ₂] (M)	[Na ₂ TeO ₃] (M)	[NaOH] (M)	[NaBH ₄] (M)	Crystallite size (nm)	BET surface area (m ² g ⁻¹)
ZnO*	0.012	0	0.15	0.5	–	18.2
ZnO*/ZnTe	0.012	0.002	0.15	0.5	–	15.0
ZnO [#] /ZnTe	0.012	0.002	0.2	0.5	–	5.6
ZnTe	0.012	0.012	0.15	0.5	60.0	29.8

*: Sheet-like nanostructure; #: rod-like nanostructure; [: concentration.

edge positions as well [26]. ZnO has been used for photocatalytic oxidation processes owing to its structural, optical and morphological characteristics [27,28]. Although it is considered an alternative of TiO₂ as the photocatalyst, only few studies have used ZnO to photoreduce CO₂ [11]. Moreover, the photoresponse is limited to the UV light due to its large band gap, which only covers ~4% of the total solar spectrum.

In addition, zinc telluride (ZnTe) is a p-type semiconductor with a direct band gap of ~2.26 eV at 300 K. It has already been used in optoelectronic devices like green light-emitting diodes and solar cells [29,30]. We have prepared mesoporous ZnTe hollow microspheres via hydrothermal method, which can photocatalytically reduce CO₂ into methane (CH₄) under visible-light irradiation with solar energy conversion efficiency of 0.072% [31]. Thus, in this work we used ZnTe to modify different ZnO nanostructures via an in situ method so as to prepare common cation heterostructures. The obtained ZnO/ZnTe heterostructures exhibit high photocatalytic capability for reduction of CO₂ into CH₄ under visible-light irradiation ($\lambda \geq 420$ nm). The conversion efficiency can even reach ~3.28% when containing ~3.35% ZnTe in terms of atomic percentage.

2. Experimental

2.1. Chemicals

All the chemicals used for fabricating ZnO/ZnTe heterostructures were of analytical grade and were used as received without any further purification. Zinc nitrate (Zn(NO₃)₂·6H₂O, ≥99%) and NaOH (≥96%) were purchased from Sinopharm Chemicals. Absolute ethanol (≥99.7%) was bought from Beijing Chemical Works. Sodium tellurite (Na₂TeO₃, ≥99.5%) and sodium borohydride (NaBH₄, ≥96%) were purchased from Alpha Aesar. Milli-Q water was used during all the experiments.

2.2. Fabrication of ZnO/ZnTe heterostructures

Typically, 0.15 M aqueous solution was prepared by dissolving 0.24 g of NaOH in 40 mL of Milli-Q water under constant stirring. Then 0.1485 g of Zn(NO₃)₂·6H₂O (0.012 M), 0.0177 g of Na₂TeO₃ (0.002 M) and 0.7566 g of NaBH₄ (0.5 M) were subsequently added into the above NaOH solution under stirring. The resultant light milky mixture was transferred into a Teflon tube, followed by being sealed in a stainless steel autoclave and kept in a microwave oven at 180 °C for 24 h. After the autoclave was cooled down at room temperature, the obtained dark brown colored precipitates via centrifugation were washed three to four times with Milli-Q water and finally with absolute ethanol. The resultant product was dried in oven at 65 °C for 8 h under vacuum. Different ZnO nanostructures have been prepared via controlling the reaction conditions (Table 1). The sheet-like ZnO was denoted as ZnO*, and the rod-like was ZnO[#]. Accordingly, the corresponding heterostructure was denoted as ZnO*/ZnTe and ZnO[#]/ZnTe, respectively.

2.3. Characterization

The crystal structure of as-prepared products has been investigated by X-ray diffraction (XRD) using Bruker D8 focus diffractometer with Ni-filtered Cu-K α radiation. The diffractograms were collected in the 2θ range of 20–80° at a scan rate of 0.1°/min. The UV–vis diffuse reflectance spectra (UV–vis DRS) were recorded using Lambda 750 UV/visible/NIR spectrophotometer with BaSO₄ as the reference and wavelength ranging from 250 to 1800 nm. The morphology, crystal structure and composition of the obtained products were analyzed by using Hitachi S4800 field-emission scanning electron microscopy (FESEM) with energy dispersive X-ray spectrometer (EDX) and Tecnai G2 F20 U-TWIN transmission electron microscopy (TEM). The valence band position of the products was determined by X-ray photoelectron spectroscopy (XPS) using ESCALAB 250Xi X-ray photoelectron spectrometer. The specific surface area was determined by Brunauer–Emmett–Teller (BET) analysis (Micromeritics, Tristar II 3020).

2.4. Photocatalytic reduction of CO₂

The photoreduction of CO₂ has been carried out using the photoreaction system described previously [31–33]. In the typical photocatalytic experiments, 10 mg of photocatalyst was used. Before the photoreduction, high purity CO₂ gas (≥99.999%) was bubbled in a quartz reactor containing 80 mL of aqueous photocatalyst suspension. The wet CO₂ was flown through the whole system for ~40 min to ensure complete removal of air from the system and the maximum adsorption of CO₂ molecules onto the active sites of the photocatalyst. A positive pressure of CO₂ was maintained at 25 kPa inside the system. Then a 300-W xenon lamp equipped with a 420 nm cut-off filter was turned on, which was kept 14–15 cm away from the upper surface of the suspension. The system was constantly recycled with tap water (15 °C) during the entire reaction using water recycling machine. The products were identified by using 7890A GC/LC system (Agilent) equipped with two (front and back) flame ionization detectors (FID) and one thermal conductivity detector (TCD) via an automated gas valve using helium (He) as the carrier gas. The product yield was determined as a function of irradiation time for a total period of 8 h. Four control experiments were performed to study whether or not the observed product was from the photoreduction of CO₂, i.e., blank reactor with and without irradiation, dark experiment with the photocatalyst, and with the same experimental conditions but using N₂ instead of CO₂. The solar energy conversion efficiency was determined by using the converted amount of fuel energy in the first 30 min relative to irradiated solar power ($\lambda \geq 420$ nm) measured with ILT 950 spectroradiometer (International Light Technology).

3. Results and discussion

3.1. Crystal structure and morphology analysis

The heterostructure is formed via an in situ hydrothermal route through a series of reactions. Zinc hydroxide (Zn(OH)₂) is formed once Zn(NO₃)₂ is added into NaOH aqueous solution. When

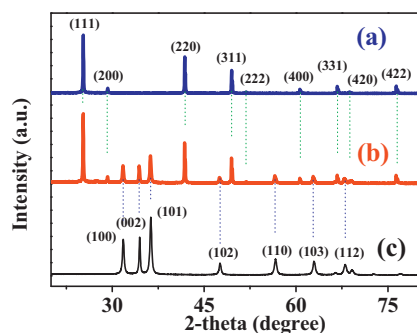


Fig. 1. XRD patterns of (a) ZnTe, (b) ZnO*/ZnTe and (c) ZnO*.

Na_2TeO_3 is added into the above alkaline solution, the obtained tellurite ions can be reduced to Te^{2-} by NaBH_4 . Here it is noted that the ratio of Na_2TeO_3 to $\text{Zn}(\text{NO}_3)_2$ in the reaction mixture is 1:6, leading to the formation of excess $\text{Zn}(\text{OH})_2$, which can react with Te^{2-} to form the ZnO/ZnTe common cation heterostructure at an optimized pH and reaction temperature.

The formation of the as-synthesized products is confirmed by XRD results in terms of the crystal structure (Fig. 1). It is evident that all the peaks for ZnTe perfectly match with the available standard diffraction pattern (powder diffraction files (PDF) number 15-0746, $a = 6.103 \text{ \AA}$) with cubic structure (Fig. 1a). All the diffraction peaks for ZnO are also accurately indexed with the standard patterns (PDF # 36-1451, $a, b = 3.25 \text{ \AA}$ and $c = 5.207 \text{ \AA}$) with wurtzite-hexagonal crystal structure (Fig. 1c). The XRD pattern confirms the formation of ZnO/ZnTe heterostructure since all the peaks from cubic ZnTe and hexagonal ZnO are present (Fig. 1b). In addition, the product is purely composed of ZnTe and/or ZnO only, as no any extra peaks can be observed corresponding to the impurities, such as elemental tellurium and/or zinc. Furthermore, the diffraction peaks in all the XRD patterns are very narrow and sharp (specifically for the ZnTe), indicating the highly crystalline nature for all the products. However, since the morphology is with irregular shape and the size is relatively large (Fig. 2), the XRD data are not used for quantitative analysis.

The SEM images of the as-prepared products are shown in Fig. 2, indicating the formation of irregular ZnTe crystals (Fig. 2a) and uniform 3D flower-like ZnO* superstructures (Fig. 2b). For

the ZnO*/ZnTe heterostructure, the ZnTe is uniformly distributed on the surface and/or inside the pores of ZnO* microstructures (Fig. 2c). It is found from the zoom-in SEM image that the flower-like 3D superstructures are composed of sheet-like petals (Fig. 2d), which are $\sim 30\text{--}40 \text{ nm}$ thick according to the ultra-high magnification SEM image (inset of Fig. 2d). It is noted that only the uniform sheet-like ZnO*/ZnTe petals are obtained at low concentration of NaOH (Fig. 2d), while the uniform flower-like hybrid superstructures composed of rod-like petals are observed (ZnO*/ZnTe) when the NaOH concentration increases from 0.15 to 0.2 M (Fig. 2e and f). This is because the NaOH may act as a structure directing agent, which is elucidated elsewhere in this work.

The formation of such hybrid microstructures can be further confirmed by TEM images (Fig. 3). For the single sheet-like ZnO*/ZnTe petals, there are some circular patches/pores on the sheet surface (Fig. 3a). The corresponding selected area electron diffraction (SAED) pattern is mainly composed of sharp diffraction points with partial formation of diffraction rings (inset of Fig. 3a), indicating the partial polycrystalline nature of these microstructures that is possibly caused by the diffusion of ZnTe onto the surface or into the pores of ZnO*. The HRTEM results reveal that ZnO*/ZnTe heterostructure is mainly composed of ZnO with $\{002\}$ as the exposed crystal facet, while for ZnTe the $\{200\}$ and $\{220\}$ facets are exposed (Fig. 3b).

For the ZnO*/ZnTe petals, their rod-like shape can also be confirmed by the TEM image (Fig. 3c), for which the partial polycrystalline nature is manifested by the SAED pattern too (inset of Fig. 3c). The ZnO $\{100\}$ crystal facet is exposed in the ZnO*/ZnTe according to the HRTEM image, while the $\{200\}$ and $\{220\}$ ZnTe facets are still exposed (Fig. 3d). The change of exposed crystal facet for ZnO in different hybrid microstructures (i.e., $\{002\}$ in ZnO*/ZnTe and $\{100\}$ in ZnO*/ZnTe) can be ascribed to the NaOH during the synthesis, which prefers to induce the growth along $\{100\}$ crystal planes of ZnO nuclei [34]. This can be further confirmed by the XRD data.

Fig. 4 represents the XRD patterns for ZnO*/ZnTe and ZnO*/ZnTe. No obvious difference can be observed between them. The change in NaOH concentration affects only two crystal planes in the XRD patterns of the hybrid microstructures, which are encircled with dotted line. In terms of the zoom-in pattern (inset of Fig. 4), it is found that the peak intensity ratio between the $\{100\}$ and $\{002\}$ crystal planes for ZnO*/ZnTe increases slightly compared

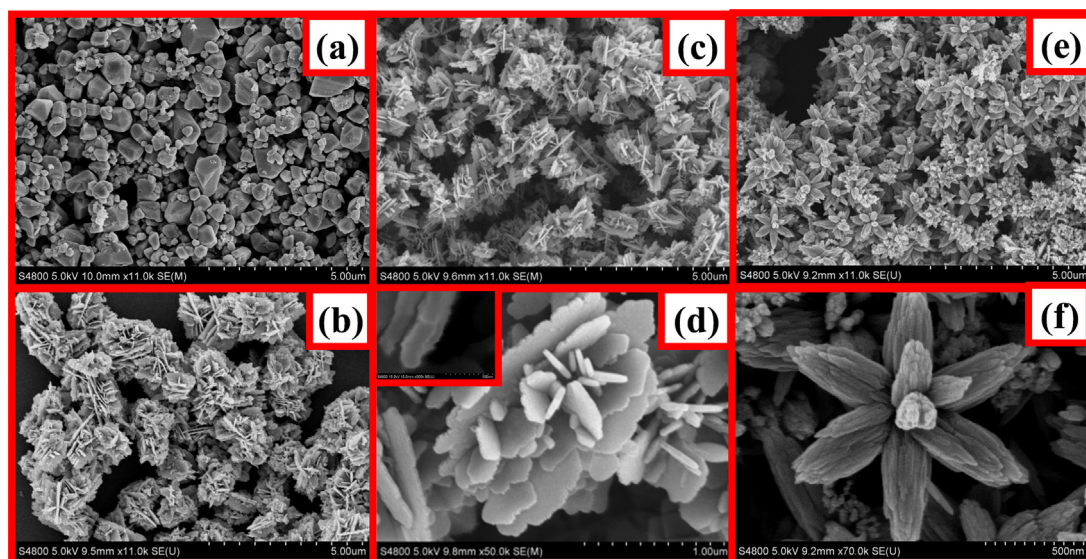


Fig. 2. SEM images of (a) ZnTe, (b) ZnO*, (c) ZnO*/ZnTe, (d) zoom-in of ZnO*/ZnTe single flower-like structure with ultra-high magnification image of single petal/sheet (inset), (e) ZnO*/ZnTe, and (f) zoom-in image of ZnO*/ZnTe single flower-like structure.

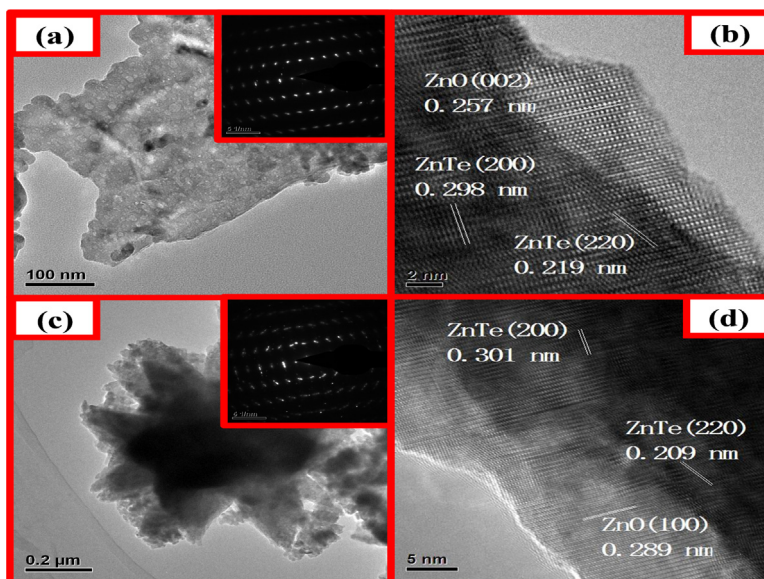


Fig. 3. (a) TEM micrograph of ZnO*/ZnTe with the SAED pattern in the inset, (b) HRTEM image for ZnO*/ZnTe, (c) TEM micrograph of ZnO#/ZnTe with the SAED pattern in the inset, and (d) HRTEM image for ZnO#/ZnTe.

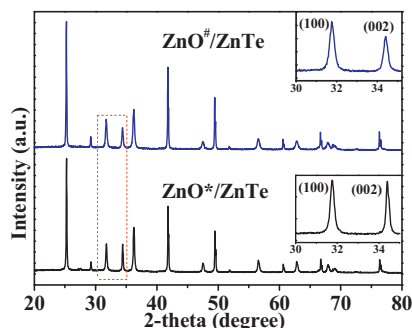


Fig. 4. XRD patterns of ZnO#/ZnTe and ZnO*/ZnTe, inset shows the respective zoom-in of (100) and (002) crystal planes.

with ZnO*/ZnTe. Thus, the increase in NaOH concentration is in favor of the growth along (100) plane, which is because the NaOH may act as the capping agent on the (002) crystal plane of ZnO, or facilitate the dissolution of ZnO along (002) plane at a high NaOH concentration as the crystal morphology is determined by the competition between the growth and dissolution of different crystal planes. This explains the formation of the rod-like features of the ZnO#/ZnTe hybrid microflowers.

EDX analysis is employed to determine the composition of ZnO* and ZnO*/ZnTe hybrid microstructures (Fig. 5). The Si signal comes from the substrate used for the EDX measurements. In case of ZnO*,

it is only composed of zinc and oxygen, and no peaks corresponding to tellurium can be observed (Fig. 5a). Besides the signals from zinc and oxygen, another two small peaks corresponding to the tellurium can be observed in the EDX spectrum for ZnO*/ZnTe (Fig. 5b), confirming the formation of the claimed heterostructure via in situ synthesis. The information obtained from EDX for selected area of the sheet-like petals of the hybrid ZnO*/ZnTe microstructure evidently reveals that it is composed of ~3.35% ZnTe and ~96.65% ZnO in terms of the atomic percentage. The amount of ZnTe in the heterostructure can be adjusted by moderately varying the ratio between Na₂TeO₃ and Zn(NO₃)₂ during the process of in situ synthesis. It is noted that the color of the as-prepared products changes from white for bare ZnO* and blackish brown for ZnTe to dark brown for ZnO*/ZnTe (Fig. 6), implying that such a small amount of ZnTe in the heterostructure may play a role similar to that for the sensitizer in dye-sensitized solar cells.

3.2. Alignment of energy levels

The activity and selectivity of a photocatalyst used for artificial photosynthesis are strongly dependent on the alignment of its energy levels, specifically the valence band (VB) and conduction band (CB) positions against SHE. Here XPS valence spectra and UV/Vis/NIR spectra have been used to determine these energy levels. The work function for the XPS instrument used in this work is 4.62 eV. Thus, the VB maximum for ZnTe, ZnO* and ZnO# is

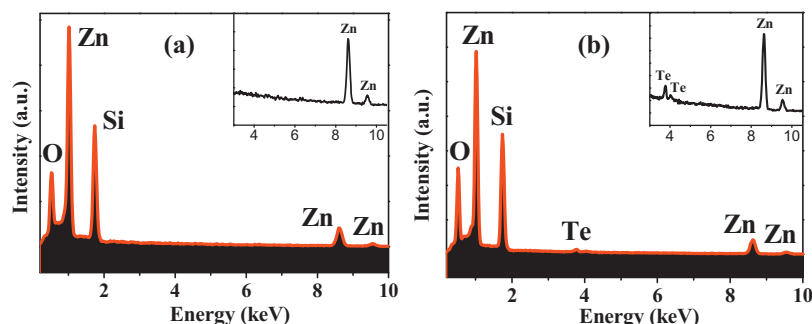


Fig. 5. EDX analysis of (a) ZnO* and (b) ZnO*/ZnTe.

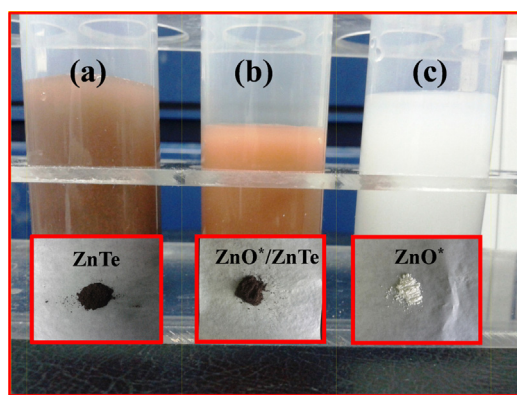


Fig. 6. Visual representation of as-synthesized (a) ZnTe, (b) ZnO*/ZnTe and (c) ZnO#.

estimated to be 5.02, 7.43 and 7.23 eV (Fig. 7), respectively (i.e., 0.42, 2.83 and 2.63 V against SHE, given 4.60 eV for 0 V).

The UV/Vis/NIR diffuse reflectance spectra for the as-synthesized ZnO*/ZnTe and ZnO#/ZnTe hybrid microstructures are shown in Fig. 8. The Kubelka–Munk function is applied for the conversion of diffuse reflectance measurements into the equivalent absorption coefficients [35]. It is clear from the inset (i) of Fig. 8a that the ZnO*/ZnTe hybrid microstructure has two strong absorption peaks, one corresponding to ZnO* at ~ 385 nm and another for ZnTe at ~ 559 nm. Similarly, ZnO#/ZnTe also exhibits two strong absorption peaks corresponding to ZnO# at ~ 388 nm and ZnTe at ~ 559 nm, respectively, as shown in the inset (i) of Fig. 8b. The band gap energy (E_g) for ZnO*, ZnO# and ZnTe in the hybrid microstructures are thus calculated via Tauc plots to be ~ 3.23 , ~ 3.21 and ~ 2.23 eV (inset (iii) of Fig. 8), respectively. So the CB minimum of ZnO*, ZnO# and ZnTe is 4.20, 4.02 and 2.79 eV, respectively. Accordingly, the alignment of energy levels for ZnO*/ZnTe and ZnO#/ZnTe hybrid microstructures can be drawn as shown in Fig. 9.

In addition, one absorption peak in the near IR region can be observed at ~ 1491 nm for ZnO*/ZnTe (inset (ii) of Fig. 8a),

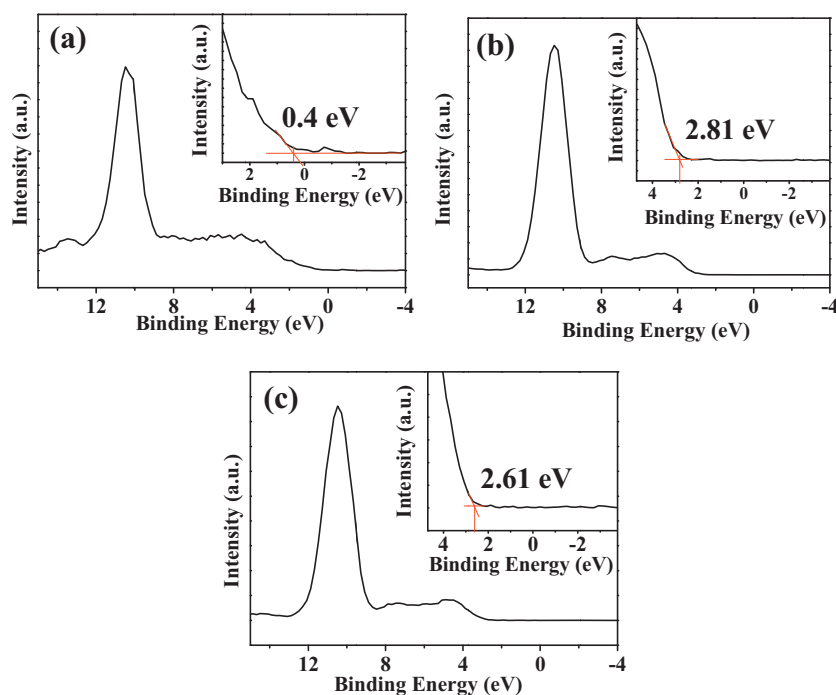


Fig. 7. XPS valence spectra for (a) ZnTe, (b) ZnO* and (c) ZnO#.

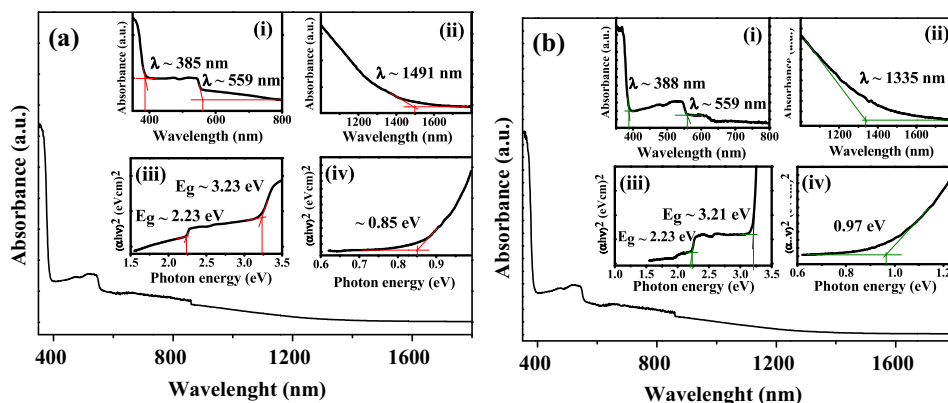


Fig. 8. UV-vis-NIR absorption spectra of (a) ZnO*/ZnTe and (b) ZnO#/ZnTe. Insets are (i) UV-vis spectrum, (ii) NIR spectrum, (iii) determination of band gap energy of ZnO and ZnTe, and (iv) determination of energy difference between VB of ZnTe and CB of ZnO.

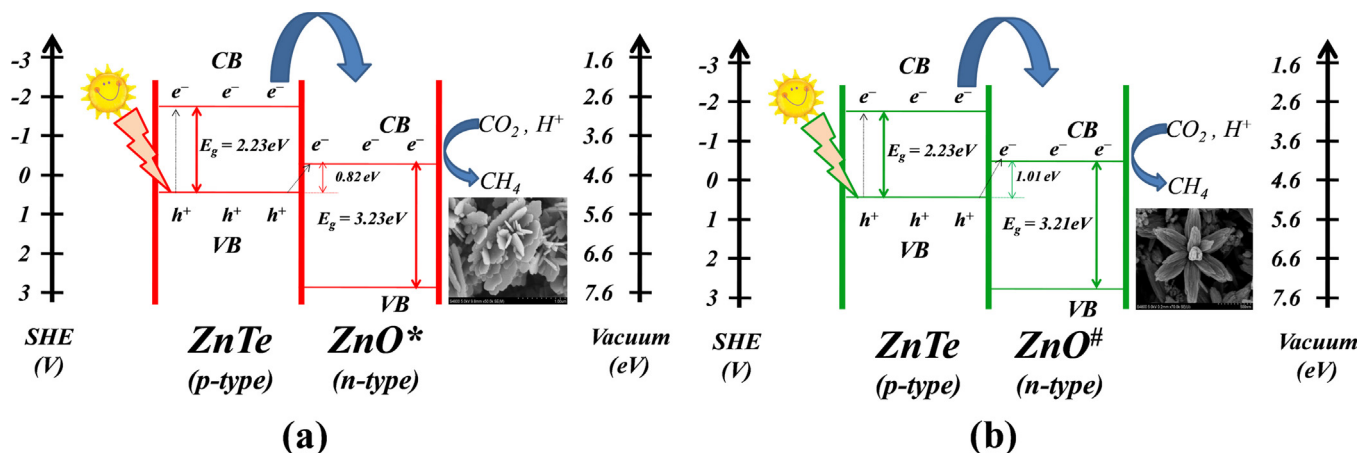


Fig. 9. Alignment of energy levels of (a) ZnO*/ZnTe and (b) ZnO#/ZnTe. The visible-light induced ($\lambda \geq 420$ nm) photoconversion of CO_2 into CH_4 is also presented here.

corresponding to an energy difference of ~ 0.85 eV (inset (iv) of Fig. 8a). This value agrees very well with the calculated energy difference between the VB of ZnTe and CB of ZnO* (0.82 eV), and is thus attributed to direct transition of electrons from the VB of ZnTe to the CB of ZnO*. In case of ZnO#/ZnTe, one absorption peak at ~ 1335 nm can be observed (insets (ii) of Fig. 8b), corresponding to an energy difference of ~ 0.97 eV (inset (iv) of Fig. 8b). Again, this value is consistent with the calculated energy difference between the VB of ZnTe and CB of ZnO# (1.01 eV), corresponding to the direct transition of electrons from the VB of ZnTe to the CB of ZnO#. Similar transition has been reported in TiO_2 –(MoO_3) system [36]. Thus, such an absorption in the near IR region strongly supports our claim for the formation of a heterostructure with strong chemical interaction between ZnTe and ZnO [36].

3.3. Photocatalytic reduction of CO_2

The as-prepared products (ZnO*, ZnO*/ZnTe, and ZnO#/ZnTe) were used to photocatalytically reduce CO_2 under the visible-light irradiation ($\lambda \geq 420$ nm). It is found that the methane (CH_4) is the major product. Four control experiments (i.e., blank reactor with and without irradiation, dark experiment with the photocatalyst, and with the same experimental conditions but using N_2 instead of CO_2) have also been carried. No CH_4 is produced for all of them (Fig. 10). Thus, the production of CH_4 indeed arises from the visible-light photoreduction of CO_2 over the synthesized photocatalysts

and not from any impurities or some external/surrounding factors. In addition, no activity for the production of CH_4 can be observed either in the case of ZnO* because ZnO is a wide gap semiconductor that only responds to the UV light (Fig. 10).

It is evident that the CH_4 can be produced upon visible-light irradiation once ZnO is combined with ZnTe (Fig. 10), no matter it is ZnO*/ZnTe or ZnO#/ZnTe. Here the ZnO*/ZnTe is used as an example to study the photoreduction activity. To figure out the suitable amount of photocatalysts for the CO_2 photoreduction under conditions used in this work, different amount of the ZnO*/ZnTe have been employed. It is found that the maximum amount of CH_4 is produced with 10 mg of the photocatalyst among the amount of 5, 10 and 20 mg (Fig. 10). The lowest yield is observed with 5 mg of the ZnO*/ZnTe, which is mainly due to the insufficient amount of the photocatalyst that is required by the photoreaction system. The system with 20 mg of ZnO*/ZnTe exhibits higher yield ($221.05 \mu\text{mol g}^{-1}$) than the one with 5 mg ($144.58 \mu\text{mol g}^{-1}$), but lower than that with 10 mg ($356.51 \mu\text{mol g}^{-1}$). This is attributed to the excess amount of the photocatalyst, which may result in agglomeration and/or poor dispersion of the photocatalyst and, thereby, lead to a relatively small number of available catalytic active sites. Thus, 10 mg is considered the optimized amount of the photocatalyst in the present photoreaction system, which is regarded to be valid for the photocatalysts of ZnO* and ZnO#/ZnTe in this work too.

3.4. Discussion of photoreduction activity

It is noted that the pure ZnTe only produces maximum of $5.67 \mu\text{mol g}^{-1}$ of CH_4 (Fig. 10), similar to the previously reported values [31,32]. The significantly enhanced production of CH_4 over the hybrid microstructures as compared to the pure ZnTe is ascribed to the formation of heterojunction between p-type ZnTe and n-type ZnO, as already mentioned above. Here it is discussed briefly based on the alignment of energy levels given in Fig. 9. Photoexcitation of a photocatalyst results in generation of charge carriers, i.e., the photogenerated electrons and holes [37]. In case of the hybrid microstructures reported here, the electrons can be excited from the VB of ZnTe into its CB upon visible-light irradiation, while leaving holes behind in the VB of ZnTe. Since the CB minimum of ZnTe (ca. -1.81 V vs SHE) is much more negative than the CB minimum of ZnO# and ZnO* (ca. -0.58 and -0.40 V vs SHE, respectively), the photogenerated electrons can efficiently transfer from the CB of ZnTe to that of ZnO (Fig. 9), as well as due to the strong interactions at the ZnO/ZnTe interface as discussed above.

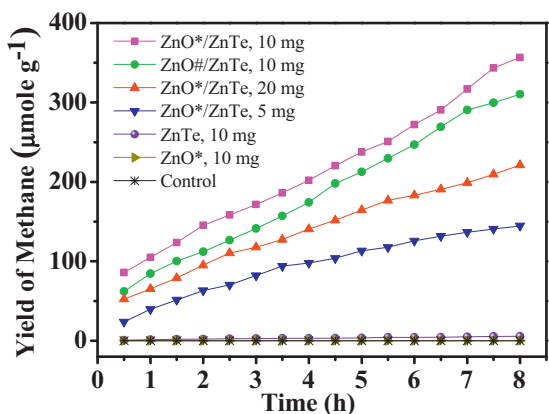


Fig. 10. Production of CH_4 as a function of time using different amount of photocatalysts.

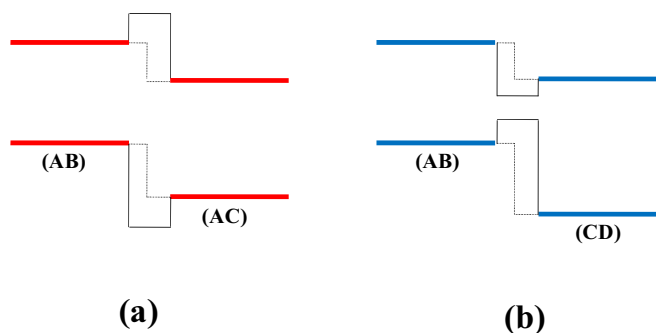


Fig. 11. Possible band alignment in type-II staggered heterojunction. (a) common cation heterostructure (i.e. AB/AC), and (b) the heterostructure without any common cation/anion.

According to the reaction mechanism [38], the electrons in the CB of ZnO can reduce CO_2 to produce CH_4 . Such an electron transfer process through the ZnO/ZnTe interface is believed to be efficient, which is faster than the recombination process of the photogenerated charge carriers due to the suitable band alignment [39]. Thus, the formation of heterostructure can facilitate the separation of photogenerated charge carriers and thus suppress the recombination. So the hybrid microstructures exhibit high activity on CO_2 photocatalytic reduction under visible-light irradiation, which is far better than the pure ZnTe.

In addition, it is noted that the common cation (Zn^{2+}) exists in both constituents in the ZnO/ZnTe heterostructure, which may play an important role in the photocatalytic activity too. If a heterostructure is formed with one common ion (e.g. AB/AC), the interface, with an energy gap larger than the band gap of the constituents (Fig. 11a), may act as an additional barrier separating the charge carriers in different layers [40]. This would definitely benefit the photoreduction activity, which is exactly the case reported in this work. On the other hand, if a heterostructure shares no any common cation or anion in its constituents (e.g. AB/CD), the interface, with an energy gap smaller than the band gap of the constituent materials, may be regarded as an ultra-thin layer of a third material that can form a quantum well which would possibly act as a

trap center for the charge carriers (Fig. 11b) [40]. This would result in decreased photocatalytic activity.

Interestingly, it is found that ZnO^*/ZnTe has higher yield of CH_4 ($356.51 \mu\text{mol g}^{-1}$) than $\text{ZnO}^\#/\text{ZnTe}$ ($310.29 \mu\text{mol g}^{-1}$) when 10 mg of the photocatalyst is used (Fig. 10). Moreover, by using the converted amount of fuel energy (calculated from the amount of CH_4 evolved in the first 30 min of photocatalysis) relative to the irradiated solar power ($\lambda \geq 420 \text{ nm}$), the solar energy conversion efficiency is calculated to be 3.28% and 2.36% for ZnO^*/ZnTe and $\text{ZnO}^\#/\text{ZnTe}$, respectively. That is to say, the ZnO^*/ZnTe exhibits higher photocatalytic activity than $\text{ZnO}^\#/\text{ZnTe}$. It is noted that the CB potential of ZnO^* (-0.40 V) is slightly less negative than that of $\text{ZnO}^\#$ (-0.58 V). In addition, the surface free energy for ZnO (002) crystal planes exposed in ZnO^*/ZnTe (9.9 eV nm^{-2}) is less than that for the (100) crystal planes exposed in $\text{ZnO}^\#/\text{ZnTe}$ (20.9 eV nm^{-2}) [41]. So the ZnO^* -based catalyst may exhibit lower activity than the $\text{ZnO}^\#$ -based one, while this is opposite to the above observed results. Thus, such difference in the CB potential and surface free energy of exposed crystal facet may contribute little to the photocatalytic reduction, or there are other factors that play a major role. Moreover, it should be pointed out that the CB potential of ZnO^* is still negative enough to reduce CO_2 to CH_4 (-0.24 V for E° at pH 7).

The first reason that accounts for the observed phenomena is that the sheet-like ZnO^*/ZnTe exhibits a higher BET surface area ($15 \text{ m}^2 \text{ g}^{-1}$) than that of the rod-like $\text{ZnO}^\#/\text{ZnTe}$ microstructure ($5.6 \text{ m}^2 \text{ g}^{-1}$). A higher surface area can provide much more active sites, resulting in higher photoreduction activity (i.e., higher CH_4 yield). In addition, the thin thickness of nano-sheet means a short transport distance for charge transfer to the surface and is thus in favor of the photocatalytic reaction thereafter [42], leading to a higher photoreduction activity than that for the nano-rod.

Though the band gap is identical for ZnTe in both ZnO^*/ZnTe and $\text{ZnO}^\#/\text{ZnTe}$ heterostructure, the energy difference between the VB of ZnTe and the CB of ZnO is less for ZnO^*/ZnTe ($\sim 0.85 \text{ eV}$) than that for $\text{ZnO}^\#/\text{ZnTe}$ ($\sim 0.97 \text{ eV}$) (Fig. 8). Owing to such an absorption via the interface, the ZnO^*/ZnTe can utilize the light energy more efficiently than $\text{ZnO}^\#/\text{ZnTe}$ with the same light source, leading to higher photocatalytic activity. Furthermore, it is noted that the CB potential for ZnTe, ZnO^* and $\text{ZnO}^\#$ is 2.79, 4.20 and 4.02 eV, respectively. The energy difference between the CB of ZnTe and the CB of ZnO is calculated respectively to be 1.41 and 1.23 eV for ZnO^*/ZnTe

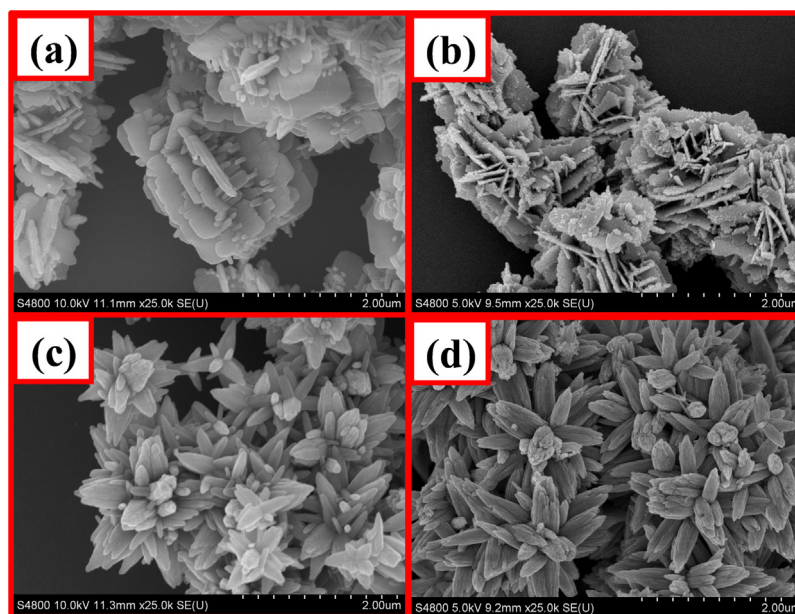


Fig. 12. SEM images of ZnO^*/ZnTe and $\text{ZnO}^\#/\text{ZnTe}$: (a) and (c) before and (b) and (d) after photoreduction, respectively.

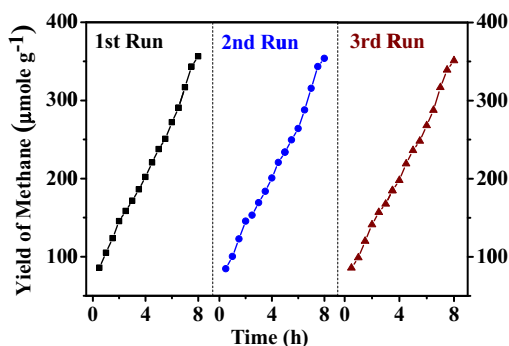


Fig. 13. Various runs for the CO₂ visible-light photoconversion into CH₄ over ZnO*/ZnTe common cation heterostructures.

and ZnO*/ZnTe. So the thermodynamic driving force for photogenerated electrons from the CB of ZnTe to that of ZnO is larger for ZnO*/ZnTe than the one for ZnO*/ZnTe. This is in favor of the electron transfer from the CB of ZnTe to that of ZnO, resulting in higher photocatalytic activity too.

The stability of the photocatalyst is also investigated here. Fig. 12 elaborates the morphological analysis before and after the photoreduction experiments. It is found that the hybrid microstructures can retain their morphology very well even after the photoreduction experiment. Furthermore, almost no change in the CH₄ yield can be observed after several runs under the visible-light irradiation (Fig. 13). Thus, the obtained photocatalysts exhibit good stability toward efficient photocatalytic reduction of CO₂.

4. Conclusions

Here the ZnO/ZnTe hybrid flower-like microstructures have been successfully synthesized via one-pot hydrothermal approach for the applications in photoreduction of CO₂ into CH₄ under visible-light illumination ($\lambda \geq 420$ nm). It is clearly noted that ZnTe is the photoactive material. The good photocatalytic activity over the hybrid microstructures is ascribed to the formation of heterojunction between ZnTe and ZnO via close interface. Sharing common cations for a heterostructure can also facilitate the activity for CO₂ photoreduction. Moreover, compared to the microstructures with rod-like petals, those with sheet-like petals have comparatively large surface area and are in favor of charge transfer to the surface, leading to higher photoreduction activity. We envision that this work may facilitate the R&D of morphologically controlled heterostructure catalysts with high photoreduction activity of CO₂ into value-added chemicals.

Acknowledgement

This work was supported by the Hundred-Talent Program of the Chinese Academy of Sciences.

References

- [1] J.D. Figueroa, T. Fout, S. Plasynski, H. McIlvried, R.D. Srivastava, *Int. J. Greenhouse Gas Control* 2 (2008) 9–20.
- [2] T. Seki, Y. Kokubo, S. Ichikawa, T. Suzuki, Y. Kayaki, T. Ikariya, *Chem. Commun.* (2009) 349–351.
- [3] M. Aresta, Wiley-VCH (2010), 1–381.
- [4] V.A. De la Pena O'Shea, J.M. Coronado, D.P. Serrano, *Dyna (Spain)* 87 (2012) 145–148.
- [5] G.R. Dey, A.D. Belapurkar, K. Kishore, J. Photochem. Photobiol. A 163 (2004) 503–508.
- [6] N. Sasirekha, S.J.S. Basha, K. Shanthi, *Appl. Catal. B* 62 (2006) 169–180.
- [7] S.S. Tan, L. Zou, E. Hu, *Catal. Today* 115 (2006) 269–273.
- [8] O.K. Varghese, M. Paulose, T.J. LaTempa, C.A. Grimes, *Nano Lett.* 9 (2009) 731–737.
- [9] V.P. Indrakanti, J.D. Kubicki, H.H. Schobert, *Energy Environ. Sci.* 2 (2009) 745–758.
- [10] G. Liu, N. Hoivik, H. Wang, H. Jakobsen, *Sol. Energy Mater. Sol. Cells* 105 (2012) 53–68.
- [11] Y. Izumi, *Coord. Chem. Rev.* 257 (2013) 171–186.
- [12] X. Feng, J.D. Sloppy, T.J. LaTempa, M. Paulose, S. Komarneni, N. Bao, C.A. Grimes, *J. Mater. Chem.* 21 (2011) 13429–13433.
- [13] C.C. Lo, C.H. Hung, C.S. Yuan, J.F. Wu, *Sol. Energy Mater. Sol. Cells* 91 (2007) 1765–1774.
- [14] K. Teramura, T. Tanaka, H. Ishikawa, Y. Kohno, T. Funabiki, *J. Phys. Chem. B* 108 (2004) 346–354.
- [15] K. Teramura, H. Tsuneoka, T. Shishido, T. Tanaka, *Chem. Phys. Lett.* 467 (2008) 191–194.
- [16] Z.Y. Wang, H.C. Chou, J.C.S. Wu, D.P. Tsai, G. Mul, *Appl. Catal. A* 380 (2010) 172–177.
- [17] S.C. Yan, S.X. Ouyang, J. Gao, M. Yang, J.Y. Feng, X.X. Fan, L.J. Wan, Z.S. Li, J.H. Ye, Y. Zhou, Z.G. Zou, *Angew. Chem. Int. Ed.* 49 (2010) 6400–6404.
- [18] Q. Liu, Y. Zhou, J. Kou, X. Chen, Z. Tian, J. Gao, S. Yan, Z. Zou, *J. Am. Chem. Soc.* 132 (2010) 14385–14387.
- [19] N. Zhang, S. Ouyang, P. Li, Y. Zhang, G. Xi, T. Kako, J. Ye, *Chem. Commun.* 47 (2011) 2041–2043.
- [20] T. Inoue, A. Fujishima, S. Konishi, K. Honda, *Nature* 277 (1979) 637–638.
- [21] M. Anpo, H. Yamashita, K. Ikeue, Y. Fujii, S.G. Zhang, Y. Ichihashi, D.R. Park, Y. Suzuki, K. Koyano, T. Tatsumi, *Catal. Today* 44 (1998) 327–332.
- [22] Y. Li, W.N. Wang, Z. Zhan, M.H. Woo, C.Y. Wu, P. Biswas, *Appl. Catal. B* 100 (2010) 386–392.
- [23] B.D. Mankidy, B. Joseph, V.K. Gupta, *Nanotechnology* 24 (2013) 405402–405408.
- [24] M. Manzanarez, C. Fabrega, J.O. Osso, L.F. Vega, T. Andreu, J.R. Morante, *Appl. Catal. B* 150–151 (2014) 57–62.
- [25] A. Bazzo, A. Urakawa, *ChemSusChem* 6 (2013) 2095–2102.
- [26] M. Grätzel, *Nature* 414 (2001) 338–344.
- [27] M.R. Hoffman, S.T. Martin, W. Choi, D.W. Bahnemann, *Chem. Rev.* 95 (1995) 69–96.
- [28] X. Chen, S. Shen, L. Guo, S.S. Mao, *Chem. Rev.* 110 (2010) 6503–6570.
- [29] Q. Wu, M. Litz, X.C. Zhang, *Appl. Phys. Lett.* 68 (1996) 2924–2926.
- [30] D.N. Bose, S. Bhunia, *J. Cryst. Growth* 186 (1998) 535–542.
- [31] M.F. Ehsan, M.N. Ashiq, T. He, *RSC Adv.* (2014) (in revision).
- [32] M.F. Ehsan, M.N. Ashiq, F. Bi, Y.Q. Bi, S. Palanisamy, T. He, *RSC Adv.* 4 (2014) 48411–48418.
- [33] F. Bi, M.F. Ehsan, W. Liu, T. He, *Chin. J. Chem.* (2014), <http://dx.doi.org/10.1002/cjoc.201400476>.
- [34] T.J. Zhu, X. Chen, Y.Q. Cao, X.B. Zhao, *J. Phys. Chem. C* 113 (2009) 8085–8091.
- [35] W.E. Vargas, *J. Opt. A: Pure Appl. Opt.* 4 (2002) 452–456.
- [36] S.H. Elder, F.M. Cot, Y. Su, S.M. Heald, A.M. Tyrshkin, M.K. Bowman, Y. Gao, A.G. Joly, M.L. Balmer, A.C. Kolwaite, K.A. Magrini, D.M. Blake, *J. Am. Chem. Soc.* 122 (2000) 5138–5146.
- [37] I.H. Tseng, W.C. Chang, J.C.S. Wu, *Appl. Catal. B* 37 (2002) 37–48.
- [38] H. Takeda, O. Ishitani, *Coord. Chem. Rev.* 254 (2010) 346–354.
- [39] L. Zhang, K.H. Wong, Z. Chen, J.C. Yu, J. Zhao, C. Hu, C.Y. Chan, P.K. Wong, *Appl. Catal. A* 363 (2009) 221–229.
- [40] C. Priester, Y. Foulon, G. Allan, *Phys. Rev. B* 49 (1994) 2919–2922.
- [41] R. Dom, H.G. Kim, P.H. Borse, *Cryst. Eng. Commun.* 16 (2014) 2432–2439.
- [42] W.G. Tu, Y. Zhou, Z.G. Zou, *Adv. Mater.* 26 (2014) 4607–4626.